



Article

Understanding the Behavior of Fully Non-Toxic Polypyrrole-Gelatin and Polypyrrole-PVdF Soft Actuators with Choline Ionic Liquids

Fred Elhi ^{1,*}, Karl Karu ^{1,2}, Pille Rinne ¹, Kadi-Anne Nadel ¹, Martin Järvekülg ³, Alvo Aabloo ¹, Tarmo Tamm ¹, Vladislav Ivaništšev ² and Kaija Põhako-Esko ¹

¹ IMS Lab, Institute of Technology, University of Tartu, Nooruse 1, 50411 Tartu, Estonia; karl.karu@ut.ee (K.K.); pille.rinne@ut.ee (P.R.); kadi-anne.nadel@ut.ee (K.-A.N.); alvo.aabloo@ut.ee (A.A.); tarmo.tamm@ut.ee (T.T.); kaija.pohako@ut.ee (K.P.-E.)

² Institute of Chemistry, University of Tartu, Ravila 14a, 50411 Tartu, Estonia; vladislav.ivanistsev@ut.ee

³ Institute of Physics, University of Tartu, W. Ostwaldi 1, 50411 Tartu, Estonia; martin.jarvekylg@ut.ee

* Correspondence: fred.elhi@ut.ee

Received: 25 April 2020; Accepted: 19 May 2020; Published: 21 May 2020



Abstract: Smart and soft electroactive polymer actuators as building blocks for soft robotics have many beneficial properties that could make them useful in future biomimetic and biomedical applications. Gelatin—a material exploited for medical applications—can be used to make a fully biologically benign soft electroactive polymer actuator that provides high performance and has been shown to be harmless. In our study, these polypyrrole-gelatin trilayer actuators with choline acetate and choline isobutyrate showed the highest strain difference and highest efficiency in strain difference to charge density ratios compared to a reference system containing imidazolium-based ionic liquid and a traditional polyvinylidene fluoride (PVdF) membrane material. As neither the relative ion sizes nor the measured parameters of the ionic liquids could explain their behavior in the actuators, molecular dynamics simulations and density functional theory calculations were conducted. Strong cation-cation clustering was found and the radial distribution functions provided further insight into the topic, showing that the cation-cation correlation peak height is a good predictor of strain difference of the actuators.

Keywords: polypyrrole; actuator; conductive polymer; gelatin; choline; ionic liquid; molecular dynamics; density functional theory; PVdF

1. Introduction

There is a high demand for versatile biofriendly materials in biomedical and soft robotics fields. Ionic electromechanically active polymer (IEAP) actuators are assured to fulfill this demand due to their attractive properties, like low operation voltage [1–3], mechanical flexibility [4], and self-sensing [5]. The IEAP actuators are also proven to be tailorable to suit the requirements by giving them the necessary shape or structure [6].

So far, these materials have shown promising performance, but applications have remained limited because of toxicity considerations. However, a typical IEAP with a three-layered structure, an ion-permeable membrane sandwiched between two porous electrodes, can be made from all biocompatible materials. Inert polymeric materials (e.g., polyvinylidene fluoride (PVdF)) or ion polymers (e.g., Nafion) usually serve as membranes, but biopolymers like gelatin [7], chitosan [8], and cellulose [9] have also been extensively studied recently. Natural origin polymers possess many favorable properties: similarity with the extracellular matrix, chemical versatility, variable mechanical properties, and biological performance without toxicity or immunological reactions. For example,

gelatin has been used in medical applications in cardiac constructions [10]. Moreover, the mechanical properties and solubility of gelatin in different environments can be tuned by crosslinking density [11]. To fabricate biofriendly electrodes, polypyrrole (PPy) as a widely used conductive polymer (CP) has been established [1] due to proven biocompatibility [12,13]. The real problem with the toxicity of the IEAP actuator lies in the choice of the electrolyte, contributing to the bending of the material.

Ionic liquids (ILs) have been incorporated successfully in IEAPs to combat the evaporation problem of the electrolyte solutions, thus enabling the actuators to work in open air. Unfortunately, many ILs have considerable toxicity issues [14]. In our previous work, we have demonstrated that this obstacle can be overcome with the right choice of ILs. We have shown that choline carboxylates are harmless towards *Escherichia coli*, *Staphylococcus aureus*, *Shewanella oneidensis* MR-1, and a HeLa cell-line, even at high concentrations, and can be used in IEAP actuators [15].

Identification of suitable components is an important step towards biofriendly IEAP actuators, but to achieve a biologically benign nature together with the high performance needed for practical applications, it is necessary to investigate the processes inside the material. The bending of the IEAP actuator comes chiefly from the ingress and egress of electrolyte ions in/out of the electrodes and through the membrane that partly acts as a reservoir for the electrolyte. The volume change of the electrodes makes the IEAP actuator bend.

A substantial amount of research has been conducted to investigate the factors contributing to the high strain difference and effectiveness of IEAP actuators. The bending beam theory [16] and numerical models [17] have been used previously, along with models taking the input voltage into account [18]. The main limitation of these models is taking into consideration only the mechanical parameters of the actuator but not the role of the electrolyte in the process. Moreover, IEAP actuators are non-linear systems [19], while many modelling studies assume uniformity. Thus, research into the behavior of ions in a PPy actuator is lacking [20]. To this end, molecular dynamics (MD) has previously been used to better understand the redox processes of PPy in IEAP actuators [21].

Because of the difficulties in the experimental determination of the processes occurring at the molecular level in IEAP actuators, computational simulations have been demonstrated to be an effective way to shed light upon this subject. For example, the dehydration of chloride ions moving deeper inside the PPy network has been observed in simulation [22]. Water seems to play a more important part in the outer layers of PPy, diminishing in influence inside deeper layers of PPy. The influence of anions grows inside the deeper layers of PPy and dehydration is compensated for by coordination of the charged sites of PPy [22,23]. The repulsion of these charged sites inside PPy also contributes to the swelling of the overall material [24].

Through simulations of ILs in a matrix, it has also been found that the volume change in the anode and cathode in a bucky-gel actuator depends on the sizes of anions and cations used, respectively [25]. The size ratio of cations and anions influences the extent of the maximum movement amplitude of the whole actuator. By extension, the maximum bending of an actuator using ILs is dependent on the amount of IL inside the actuator [26]. In related research it has been found that higher electromechanical conversion efficiency for ionic polymer-metal composites is achieved when only a fraction of the ions inside the actuator are free to move along stationary counterions [27]. The results previously mentioned illustrate the importance of ionic interactions inside the IEAP structure. It naturally follows that besides developing a biologically benign actuator system, we also need to know how the functional groups of the IL interact with water, the membrane, and the electrodes to tailor the behavior of the actuator.

In the present study, PPy-gelatin actuators containing three different choline ILs were studied to investigate the capabilities of biofriendly actuators and to compare them to actuators with a traditional commercial PVdF membrane, synthesized and characterized electro-chemo-mechanically and mechanically with the same methods. The characterization included the disk diffusion test to confirm the biofriendliness of the PPy-gelatin actuators. IEAP actuators are complex systems and it is often difficult to predict the exact behavior of the electrolyte and how well its properties will be converted to strain difference. Therefore, the current study seeks to explain the empirical results with

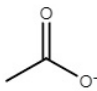
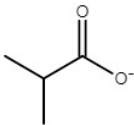
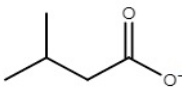
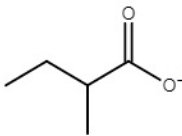
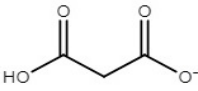
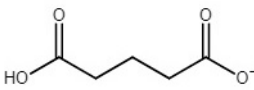
computational methods. The formation of ionic clusters was studied with MD simulations and with density functional theory (DFT) calculations.

2. Materials and Methods

2.1. Preparation of PPy-Gelatin Actuators

PPy-gelatin actuators were made using the electrochemical deposition of PPy on gelatin membranes and afterwards immersing the laminates in choline IL (Table 1). The synthesis process of the three choline ILs used in this research as well as the three additional ones, to put the results in a wider context, and their corresponding properties have been reported previously [15].

Table 1. Choline ionic liquids (ILs) used in this research.

Ionic Liquid	Anion Structure
choline acetate ([Ch][Ac])	
choline isobutyrate ([Ch][Ib])	
choline isovalerate ([Ch][Iv])	
choline 2-methylbutyrate ([Ch][2mb])	
choline malonate ([Ch][Mal])	
choline glutarate ([Ch][Glu])	

2.1.1. Preparation of Gelatin Membranes

The gelatin membranes were prepared by electrospinning from acetic acid solution and crosslinking with glucose, which helps to enhance the mechanical properties and achieve insolubility in an aqueous environment without compromising biocompatibility. Gelatin (Sigma-Aldrich, St. Louis, MO, USA; Type-A, Bloom number: 300 g) and D-(+)glucose (Sigma-Aldrich, St. Louis, MO, USA) powders were mixed in the weight ratio 17:3, because a too high glucose content can result in brittle fibers [11]. The mixture was then dissolved in 10 M acetic acid (Sigma-Aldrich, St. Louis, MO, USA; 99.8%) by vigorous stirring for 30 min at 40 °C to obtain a 25% polymer solution. Electrospinning was carried out under ambient conditions using a horizontal electrospinning device. The setup consisted of a high voltage power supply (Heinzinger LNC 3000, Heinzinger electronic GmbH, Rosenheim, Germany; voltages in the range of 0–30 kV), stationary collector, syringe pump (New Era Pump Systems NE-511; Farmingdale, NY, USA), syringe, and a needle (Injekt-F, Braun; Melsungen, Germany). The solution was pumped through a 0.6 mm needle at 8 μ L/min and collected on a plate 20 cm away from the tip. The working voltage was 19 kV. Crosslinking of the obtained glucose-gelatin fibers was carried out at 175 °C for 1.5 h [11,28]. The gelatin membranes (thickness: 110 μ m) had a very low density (void volume 65%).

The ionic conductivities of the gelatin membranes immersed in ILs were determined using a method described previously [15]. The measurements of the ionic conductivities of the ILs were carried out using a Micrux microfluidic chip with interdigitated gold electrodes. Parstat 2273 potentiostat-galvanostat (Princeton Applied Research, Oak Ridge, TN, USA) was used for the electrochemical impedance spectroscopy measurements for a drop of each IL, which in turn were used to calculate the ionic conductivities of the choline ILs. The impedance was determined from both low to high frequency and from high- to low-frequency scans, six times for each IL. To evaluate the influence of humidity on the conductivity of the ILs, the impedance was also measured at different time points: right after synthesis and after 10 min under ambient conditions.

2.1.2. Electrochemical Synthesis of PPy Electrodes

The electrochemical synthesis of PPy electrodes on gelatin membranes was done by adapting the method established in our previous publications [15,29]. To make the membrane surface conductive for electrochemical synthesis, the gelatin membranes were coated with a 20 nm gold layer using a Leica EM ACE600 sputter coater (Leica Mikrosysteme GmbH, Vienna, Austria).

PPy doped with dodecylbenzenesulfonate was deposited on both sides (30 mm × 30 mm) of the gelatin membrane galvanostatically using a PARSTAT 2273 potentiostat/galvanostat, in a one-compartment electrochemical cell at $-23\text{ °C} \pm 2\text{ °C}$. The applied current density was $0.1\text{ mA}\cdot\text{cm}^{-2}$ for 20,000 s. The gold-coated gelatin membrane served as the anode and the symmetrical stainless steel (AISI 316L) mesh sheets served as the cathodes.

The synthesis solution was comprised of 0.2 M pyrrole (Py) (Sigma-Aldrich, St. Louis, MO, USA; distilled at reduced pressure before use) and 0.2 M sodium dodecylbenzenesulfonate (NaDBS) (Sigma-Aldrich, St. Louis, MO, USA; technical grade), which were dissolved in a mixture of MilliQ water and monoethylene glycol (MEG) (Fluka, Charlotte, NC, USA; 99% purity) at a volume ratio of 1:1. The PPy-coated gelatin laminates were washed with ethanol and MilliQ water and dried at room temperature at lowered pressure (1 mbar) for 24 h. The 3 mm × 14 mm strips cut from the synthesized PPy-gelatin sheets were immersed in the ILs (Table 1) for at least 72 h before electromechanical characterization.

To study the morphology of the PPy-gelatin actuators, the samples were broken in liquid nitrogen. A Hitachi TM3000 microscope (Tokyo, Japan; acceleration voltage of 15 kV, back-scattered electron detector) was used for the cross-sectional imaging; an Oxford Instruments SwiftED 3000 EDX analyzer (Abingdon, UK) was used for X-ray sulfur mapping.

2.2. Electro-Chemo-Mechanical Characterization of PPy-Gelatin Actuators

The PPy-gelatin actuators were characterized electro-chemo-mechanically [15,30] with 2 mm of the actuators fixed sideways between gold contacts. A laser displacement meter was used to measure the actuator displacement at 5 mm from the fixed end. The actuators were driven using 3 different types of signals: a square wave potential steps signal between $\pm 1\text{ V}$ at 0.001 Hz, with neutral voltage intervals between polarization steps, and triangular voltage signals between $\pm 1\text{ V}$ with scan rates of $5\text{ mV}\cdot\text{s}^{-1}$ and $50\text{ mV}\cdot\text{s}^{-1}$. Maximum strain differences were calculated relative to the middle position of a full bending cycle according to the formula [30]:

$$\varepsilon = \frac{2 \cdot D \cdot W}{L^2 + D^2} \quad (1)$$

where ε is the strain difference, D is half of the peak to peak displacement from the graph, W is the thickness of the actuator (assuming constant thickness), which was measured with a micrometer, and L is the distance from the fixed end of the actuator to the projection of the laser beam at the middle position of the actuator.

Charge efficiency for the PPy-gelatin and the previously published PPy-PVdF [15] actuators was calculated by dividing their maximum strain difference by charge density of the driving signal.

To test the durability of PPy-gelatin actuators at a high-frequency driving signal (400 Hz), a frequency response test was carried out. For this, the actuators were characterized using a mirrored logarithmic sweep sine signal from 0.001 Hz to 400 Hz, with an amplitude of ± 1 V.

PARSTAT 2273 potentiostat/galvanostat was used to measure the cyclic voltammetry (CV) response of the actuators in a two-electrode system. Five cycles in the range of ± 1 V at scan rates of $5 \text{ mV}\cdot\text{s}^{-1}$ and $50 \text{ mV}\cdot\text{s}^{-1}$ were recorded.

For mechanical characterization, the synthesized PPy actuators were mounted side-ways between two gold Kelvin clip contacts. The resonance frequency of the mechanically excited oscillating actuator was measured for three different free lengths using a laser displacement meter. The equivalent elastic modulus of the composite was calculated from this data [31].

All measurements described here were carried out under ambient conditions (35.5 RH%, 25 °C, normal atmospheric pressure). To ensure comparison of the results, the PPy-gelatin actuators were characterized similarly to the PVdF-PPy actuators.

2.3. Microbial Compatibility of PPy-Gelatin Actuators

The disk diffusion method [15,32,33] was used to assess the harmlessness of PPy-gelatin actuators towards an Uropathogenic strain of *E. coli* (CFT073). Three choline ILs were used for PPy-gelatin actuator testing and three additional choline ILs were used.

Ultraspex 7000 (Biochrom LTD, Cambridge, UK) was used to adjust the density of the initial *E. coli* suspension to 0.5 McFarland standard ($A_{600} = 0.063$; between 1×10^8 and $2 \times 10^8 \text{ CFU}\cdot\text{ml}^{-1}$) using a 600 nm wavelength.

Lysogeny broth agar served as the substrate for bacterial growth and the *E. coli* suspension was smeared on its surface. 4×4 mm squares of IL-immersed actuator material were placed on the surface of the inoculated agar with sterilized forceps. As negative controls, the following ILs widely used in IEAPs were applied: 1-ethyl-3-methylimidazolium trifluoromethanesulfonate ([EMIM][OTf]) (Solvionic, Toulouse, France; purity > 99.5%), 1-ethyl-3-methylimidazolium bis(fluorosulfonyl)imide ([EMIM][FSI]) (Solvionic, Toulouse, France; purity > 99.5%), and 1-ethyl-3-methylimidazolium bis(trifluoromethylsulfonyl)imide ([EMIM][TFSI]) (Fluka, Charlotte, NC, USA; purity > 98%). The plates were incubated at 37 °C for 22 h and afterwards photographed on a black non-reflecting background to assess their inhibition halo diameters. This experiment was carried out in triplicates.

2.4. Computational

In this work, the studied ILs were investigated with molecular dynamics (MD) simulations and with density functional theory (DFT) calculations. For the former, averaged atomic partial charges were fitted.

2.4.1. Molecular Dynamics Simulations

The MD simulations were conducted with Gromacs 5.1.4 [34] software and the OPLS-AA force field [35]. The partial charges were refitted, as described in Section 2.4.2. The simulation boxes consisted of 400 ion pairs and water packed with the Packmol algorithm [36] (Supplementary Material: Figures S1 and S2).

First, steep energy minimization was performed, followed by an isochoric-isothermal (NVT) equilibration run of 0.2 ns. Then, a 2 ns production run was conducted in the isobaric-isothermal (NPT) ensemble at 1 bar pressure. All simulations were done at 298.15 K with 3-dimensional periodic boundary conditions. The simulations employed particle-mesh Ewald electrostatics [37], a v-rescale temperature coupling algorithm, and isotropic Berendsen pressure coupling with time constant 0.5 ps [38].

2.4.2. Partial Charges

The initial atomic charges were generated from CHELPG (Charges from Electrostatic Potentials using a Grid-based method) electrostatic charges [39] of single ions, which were calculated with Perdew–Burke–Ernzerhof exchange–correlation functional (PBE) and Ahlrichs split-valence basis set with polarization on heavy atoms (def2-SVP) [40–42]. The DFT calculations were carried out with an Orca 4.0.0.2 quantum chemical program suite [43]. These charges were used in preliminary 2 ns NPT simulations.

For each IL, eight snapshots were extracted from the resulting trajectories and fed to Geometry, Frequency, Noncovalent, eXtended Tight-Binding method (GFN-xTB) program package [44]. GFN-xTB yields Hirshfeld charges, which are used to find averaged atomic charges for all atom types. As the GFN-xTB calculation is not periodic, ions with an incomplete solvation shell were excluded from the charge estimation process. The obtained charges were used in further simulations.

2.4.3. Molar Volume of Ions

The starting geometries for the studied ions were obtained by first performing a simulated annealing based conformer search for the corresponding ionic pairs with the GFN-xTB tight-binding semi-empirical program package [44]. The counter-ion for each of the anions was choline, and the counter ion for choline was bis(trifluoromethylsulfonyl)imide ([TFSI][−]).

The lowest energy conformer for each IL pair was further optimized with Orca 4.0.0.2 [43] at the PBE/def2-SVP level of DFT [40–42]. The geometries of the individual ions were obtained by removing the counter ions from the ionic pair geometries. The ion sizes were then estimated using V_m^1 and V_m^2 methods.

For the V_m^1 method, a single point calculation of the ions was performed with Gaussian 09 [45] at the B3LYP/def2-tzvp level of DFT [41,42,46,47] with a fine integration grid (as defined in Gaussian 09). The volume of the ions was estimated from the single point calculation as the volume, where the electron density surpasses 0.001 electrons/Bohr³.

For the V_m^2 method, the geometry of each ion was aligned along the principal axes using the Reorient package of VMD [48]. Orthorhombic boxes, with faces parallel to the *xy*-, *yz*-, and *xz*-coordinate planes, were fitted around the ions as tightly as possible. Van der Waals radii from Bondi [49] were used to estimate the sizes of atoms during the fitting. The resulting box sizes are reported as ion volumes.

3. Results and Discussion

The objective of this research was to investigate the various aspects of the behavior of IEAP actuators made from biologically benign choline ILs, PPy, and gelatin. Furthermore, the interactions between functional groups of the materials were a topic of interest. Initially, the ionic conductivities of the chosen choline ILs were determined in pure form and in the gelatin membrane. Furthermore, the ILs were used in PPy-gelatin actuators, which were characterized morphologically and electro-chemo-mechanically. The obtained results were compared with those of the standard PPy-PVdF actuators containing the same choline ILs as electrolytes [15]. In addition, the biological impact of the PPy-gelatin actuators was assessed with a disk diffusion experiment. Finally, the molar volumes were calculated and the radial distribution of the mobile particles in IEAP actuators was assessed to explain the experimental results.

3.1. Ionic Conductivities of Choline ILs in Gelatin Membranes

In Table 2 the ionic conductivities of all the chosen choline ILs and the gelatin membranes saturated with the ILs are presented. Ionic conductivity is an important variable for obtaining a high-performance actuator because of the mobility of ions and their interaction with the membrane.

Table 2. Ionic conductivities (κ) of ILs in membranes. The conductivity was measured right after immersing the membrane materials into ILs in an inert atmosphere and after 10 min in ambient conditions.

Ionic Liquid	Ionic Conductivity of ILs in Membranes $\kappa/\text{mS}\cdot\text{cm}^{-1}$	
	Gelatin	Gelatin, 10 min
[Ch][Ac]	0.48	1.65
[Ch][Ib]	0.06	0.28
[Ch][Iv]	0.06	0.18
[Ch][2mb]	0.01	0.40
[Ch][Mal]	0.05	0.26
[Ch][Glu]	0.00	0.16

In all cases, pure ILs, in PVdF membrane [15] and in the gelatin membrane, [Ch][Ac] had the highest ionic conductivity and [Ch][Glu] the lowest. Thus, the ionic conductivities in the membranes were primarily determined by the ILs the membrane had been immersed in. In ambient conditions, the conductivities increased in time due to the absorbed water from the atmosphere. Similar kinds of correlations were determined before for PVdF membranes [15], but comparison of the results indicates that in gelatin membranes higher conductivities can be achieved. Similarly to the present study, the highest ionic conductivity in PVdF membrane was exhibited for [Ch][Ac] (0.44 and $0.55 \text{ mS}\cdot\text{cm}^{-1}$ in an inert atmosphere and after 10 min in ambient conditions, respectively), and the lowest ionic conductivity was observed in the case of [Ch][Glu] (below detection and $0.02 \text{ mS}\cdot\text{cm}^{-1}$ in an inert atmosphere and after 10 min in ambient conditions, respectively). Directly after immersion, the conductivities of both PVdF and gelatin membranes were similar, but after 10 min under ambient conditions, the conductivities of the gelatin membranes were significantly increased due to the more hygroscopic nature.

3.2. Structure and Morphology of PPy-Gelatin Actuators

PPy-gelatin actuators were realized by the electrochemical synthesis of PPy on electrospun gelatin membranes, after which the obtained laminates were immersed in the ILs. The overall thickness of the actuators did not increase significantly after swelling in ILs and under ambient conditions. The thicknesses remained around $130 \mu\text{m}$. The mass of the laminates, on the other hand, increased by about 75%. SEM micrographs of the cross-sections (Figure 1) reveal that the PPy layer on top of the gelatin membrane follows the fibrous structure inherited from the electrospinning. There is also a denser structure visible in the middle of the gelatin membrane, probably formed by fusing of partially dried fibers during the thermal treatment of uncoated gelatin mats, as it was present already before the PPy synthesis and immersion step (Supplementary Material: Figure S3). EDX sulfur mapping was used to investigate the PPy layer further, featuring the distribution of $[\text{DBS}]^-$ anions in the materials. A higher concentration of $[\text{DBS}]^-$ anions in the outer layers of the actuators indicates the presence of PPy. The EDX sulfur mapping confirmed that in PPy-gelatin actuators, PPy was deposited through the fibrous layers up to $40 \mu\text{m}$ deep. A rather different kind of structure than the PPy layer on top of the PVdF membrane, which appears thinner ($2\text{--}3 \mu\text{m}$) and more uniform [15] than that on the gelatin membranes.

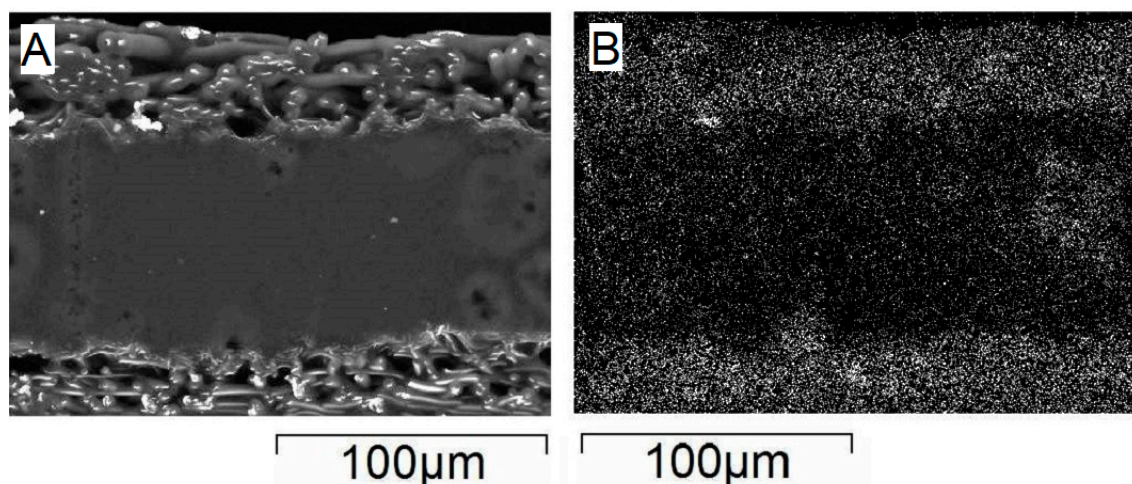


Figure 1. SEM image of the cross-section (A) and EDX sulfur map (distribution of $[\text{DBS}]^-$ anions) (B) of a PPy-gelatin actuator.

3.3. Electro-Chemo-Mechanical Properties of PPy-Gelatin Actuators

The maximum displacement of actuators is one of their primary characteristics, and the methods used to measure it in this study are described in Section 2.2. $[\text{EMIM}][\text{OTf}]$ was used as a reference to compare choline-ILs against, as it represents conventionally used imidazolium-based ILs. Three choline ILs were chosen for the preparation of PPy-gelatin actuators based on the results of PPy-PVdF actuators [15] and the ionic conductivities measured in gelatin membranes (Table 2): $[\text{Ch}][\text{Ac}]$ and $[\text{Ch}][\text{Ib}]$ as high-performance ILs, $[\text{Ch}][\text{Mal}]$ as a low-performance IL, and additionally $[\text{EMIM}][\text{OTf}]$ as the reference. Table 3 summarizes the results and compares them with the previously obtained ones for PPy-PVdF actuators with the same choline ILs. In both cases, the highest maximum strain difference values were achieved with the actuators containing $[\text{Ch}][\text{Ac}]$ or $[\text{Ch}][\text{Ib}]$ as the electrolytes. All the studied ILs in PPy-gelatin actuators showed dominant cationic activity.

While the flux of ions (induced by the exchanged charge) drives the actuation, the mechanical properties of the actuators influence the performance significantly. Therefore, the elastic moduli were determined from the resonance frequencies of the mechanically excited oscillating actuators (Table 3). In general, the PPy-gelatin actuators were less stiff than the previously tested PPy-PVdF actuators, but the elastic moduli were found to be influenced by the IL as well. Actuators with $[\text{Ch}][\text{Ac}]$ and $[\text{Ch}][\text{Ib}]$ showed the lowest elastic moduli (Table 3).

Table 3. Strain difference (%) calculated according to (1). sq—actuators driven with square wave voltage ± 1 V at 0.001 Hz; CV 5—actuators driven with triangle wave CV signal ± 1 V at $5 \text{ mV}\cdot\text{s}^{-1}$; CV 50—actuators driven with triangle wave CV signal ± 1 V at $50 \text{ mV}\cdot\text{s}^{-1}$.

Ionic Liquid	PPy-Gelatin				PPy-PVdF			
	Strain Difference/%			Elastic Modulus/MPa	Strain Difference/% [15]			Elastic Modulus/MPa
	sq	CV 5	CV 50		sq	CV 5	CV 50	
$[\text{Ch}][\text{Ac}]$	0.62 ± 0.12	1.35 ± 0.13	0.17 ± 0.03	61	0.67 ± 0.09	0.65 ± 0.05	0.30 ± 0.03	186
$[\text{Ch}][\text{Ib}]$	0.29 ± 0.12	1.79 ± 0.14	0.34 ± 0.07	94	0.19 ± 0.08	0.49 ± 0.07	0.15 ± 0.05	221
$[\text{Ch}][\text{Mal}]$	0.18 ± 0.09	0.09 ± 0.01	0.03 ± 0.01	301	0.11 ± 0.02	0.06 ± 0.01	0.02 ± 0.00	990
$[\text{EMIM}][\text{OTf}]$	0.07 ± 0.01	0.05 ± 0.01	0.03 ± 0.00	222	0.16 ± 0.02	0.05 ± 0.01	0.04 ± 0.01	914

Besides the different ILs as the electrolytes, gelatin was compared to PVdF as the membrane material. Membranes influence the performance of actuators through mechanical properties; elasticity, for example, is one of the parameters influencing the strain difference. All PPy-gelatin actuators showed lower elastic moduli than the corresponding PPy-PVdF ones, which also correlates with the higher strain difference values (Table 3). It was also found that the optimal driving signal was different for different membranes and ionic liquid combinations. In general, CV 50 was never the

highest-strain option, while the square wave signal gave the highest strain for PPy-PVdF actuators. PPy-gelatin actuators showed no clear trend, and the performance was more influenced by the specific electrolyte used: ILs with smaller anions like [Ch][Ac] and [Ch][Ib] showed higher strain differences when driven by the slower CV, whereas the bulkier [Ch][Mal] and [EMIM][OTf] showed larger strain difference values with square wave potential steps. On the one hand, the square wave potential steps signal reduces one electrode of the actuator too quickly, and thus, the actuator loses electronic conductivity, while in the case of the triangular signal, both the voltage and current increase steadily and facilitate motion of the ions more gradually. On the other hand, square wave steps generate much larger local electric fields, capable of pushing and pulling localized ions. Hence, the triangular signal favors thermodynamic control, while the square wave generates situations much further away from equilibrium and facilitates kinetic control. As seen from Table 4, the actuators with [Ch][Ac] and [Ch][Ib] achieve higher strain difference values without consuming more charge than actuators containing other ILs. It can also be seen that the triangular driving voltage signal is more effective in driving the actuators than the square wave potential steps. Overall, PPy-gelatin actuators turn more charge into more displacement. Therefore, in combination with PPy electrodes and choline ILs, gelatin is the preferred membrane material over PVdF.

Table 4. The charge-efficiency of the tested actuators (%·Coulomb⁻¹·cm²), defined as the strain difference (%) divided by charge density (Coulomb·cm⁻²). sq—actuated with square wave voltage; CV 5 and CV 50—actuated with triangle wave CV signal with 5 mV·s⁻¹ and 50 mV·s⁻¹, respectively.

Ionic Liquid	PPy-PVdF sq	PPy-PVdF CV 5	PVdF-CV CV 50	PPy-Gelatin sq	PPy-Gelatin CV 5	Gelatin-CV CV 50
[Ch][Ac]	10	11	12	16	74	77
[Ch][Ib]	5	11	12	13	81	85
[Ch][Mal]	3	3	2	2	5	4
[EMIM][OTf]	5	5	5	6	8	8

Cyclic voltammetry can reveal important information about the characteristics of IEAP actuators. The actuators in the present study did not exhibit a noteworthy change in the CV surface area from cycle to cycle, once already in ambient conditions. Thus, the second cycle of CVs for PPy-gelatin actuators are presented in Figure 2. With gelatin membranes, there was a noticeable scan-rate dependence, but not as much as with PPy-PVdF actuators, which indicates a wider useful response window. Perhaps the most outstanding is the response of [Ch][Ac], where the shape of the voltammogram was clearly changed but without losing much in overall exchanged charge (Table 4). In our previous study [15] of actuators with PVdF membranes, neither [Ch][Mal] nor [EMIM][OTf] showed significant dependence on scan rate, while other ILs were incapable of keeping up with the faster scan rate.

Charge-efficiency in the case of different driving signals is compared in Table 4. It is again noteworthy that the significantly lowered exchanged charge with increased scan rate in the case of PPy-gelatin had virtually no (negative) effect on the charge efficiency, pointing at very strong coupling between the ion flux (charge) and the mechanical response (actuation).

The frequency response testing with the mirrored signal showed that the displacement of the actuators was similar even after being driven with a high-frequency signal (Supplementary Material: Figures S4 and S5). This indicates that the materials did not lose their properties even after being actuated at high frequencies.

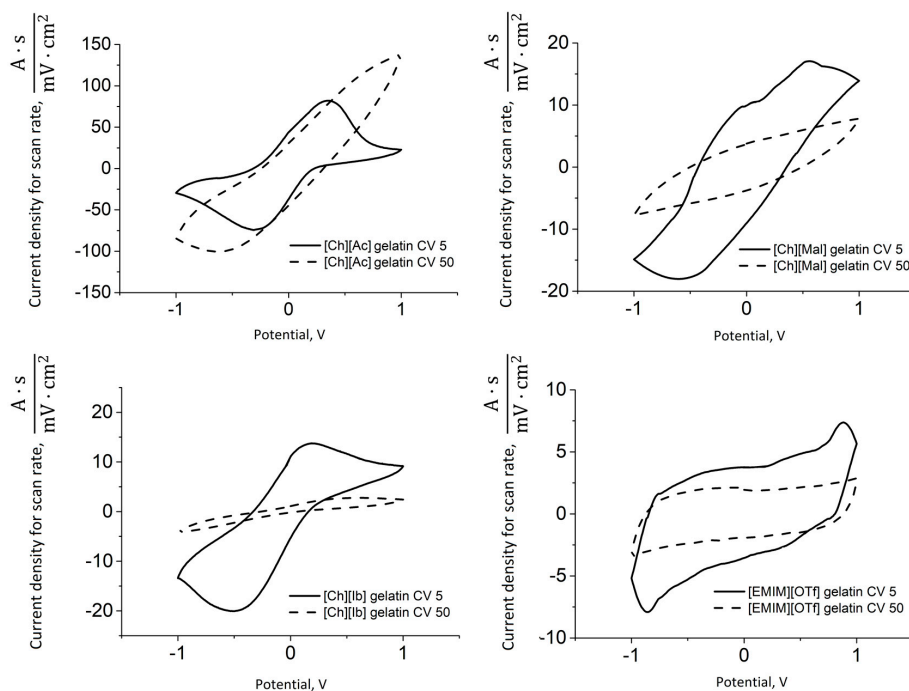


Figure 2. Cyclic voltammetry results for PPy-gelatin actuators. Solid lines for scan rates of $5 \text{ mV}\cdot\text{s}^{-1}$; dashed lines for $50 \text{ mV}\cdot\text{s}^{-1}$.

3.4. Biological Impact of PPy-Gelatin Actuators

Even when the individual components of a composite exhibit no harmful effect towards living organisms, they might act differently when combined. Therefore, the disk diffusion tests were conducted to assess the harmless nature of the prepared actuators.

ILs can affect the pH of the agar medium, thus harming the test organisms. Diffusion through the medium and the microbial cell wall is also possible. Both of these mechanisms of inhibition are possible if the experiment shows areas with no microbial growth around the samples. From the results in Figure 3, no inhibition rings around actuator samples can be seen. Choline ILs showed no inhibition towards *E. coli* when combined with PPy-PVdF actuators. It concludes that choline ILs containing PPy-gelatin samples are benign towards *E. coli*.

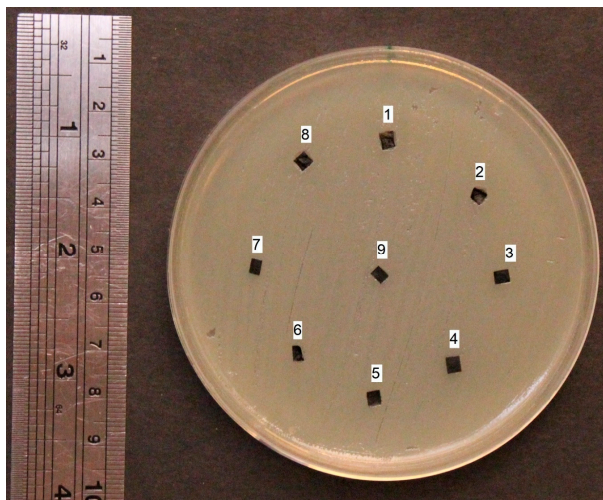


Figure 3. Results for PPy-gelatin actuator disk diffusion test of *E. coli* assay. Positions: 1—[Ch][Ib], 2—[Ch][Iv], 3—[EMIM][FSI], 4—[Ch][Mal], 5—[Ch][Ac], 6—[Ch][2mb], 7—[EMIM][OTf], 8—[Ch][Glu], 9—[EMIM][TFSI].

3.5. IL Properties Governing Actuation

Choline ILs were studied through simulations before [50], but to shed light on the differences in their performance in actuators, new MD and DFT simulations have been conducted.

Ion sizes of the ILs were calculated and their interactions described with simulations to give insight into the properties governing the actuation processes inside the actuators. Ion sizes of the ILs were calculated to explain their electrolyte properties. Ion sizes calculated with the Vm^1 method varied from $49 \text{ cm}^3 \cdot \text{mol}^{-1}$ to $109 \text{ cm}^3 \cdot \text{mol}^{-1}$, while Vm^2 showed larger values ranging from $71 \text{ cm}^3 \cdot \text{mol}^{-1}$ to $179 \text{ cm}^3 \cdot \text{mol}^{-1}$ (Table 5). $[\text{Ac}]^-$ is clearly the smallest anion with either method, while $[\text{2mb}]^-$ and $[\text{Glu}]^-$ are the two larger ones. However, the mobility of ions in the actuators is influenced not only by the molar volumes but also by the shapes of the ions, described using the different closest-fitting box side dimensions (Table 5).

Table 5. Molar volumes and closest-fitting box dimensions of the ions in the ILs.

Ion	Vm^1 ($\text{cm}^3 \cdot \text{mol}^{-1}$)	Vm^2 ($\text{cm}^3 \cdot \text{mol}^{-1}$)	x (Å)	y (Å)	z (Å)
$[\text{Glu}]^-$	109	171	5.50	6.78	7.60
$[\text{2mb}]^-$	108	175	5.31	6.60	8.27
$[\text{Mal}]^-$	88	122	4.55	5.78	7.68
$[\text{Ch}]^+$	84	179	6.05	6.32	7.78
$[\text{Iv}]^-$	84	165	5.45	5.92	8.47
$[\text{Ib}]^-$	65	145	5.27	6.72	6.78
$[\text{OTf}]^-$	63	107	5.66	5.52	5.71
$[\text{Ac}]^-$	49	71	4.09	5.31	5.42

The relation between the IL properties and the performance of the actuators is not obvious from the experimental results and calculated ion sizes. As a first approximation, strain difference should correlate with ion size—larger migrating particles should cause a larger displacement. Another important factor is the ionic conductivity of the electrolyte. As actuation is not an equilibrium process, a more conductive electrolyte should produce a larger strain. Based on the results above, the differences in actuator performance cannot be entirely explained with the studied IL properties—although there is a moderate negative correlation between the anion size and the ionic conductivity of the ILs (Figure 4), neither the ion dimensions nor the ionic conductivities correlate strongly with strain difference and are, therefore, not sufficient to explain the dramatic change of the strain difference results of actuators with $[\text{Ch}][\text{Ib}]$, compared to actuators with $[\text{Ch}][\text{Mal}]$ and $[\text{EMIM}][\text{OTf}]$.

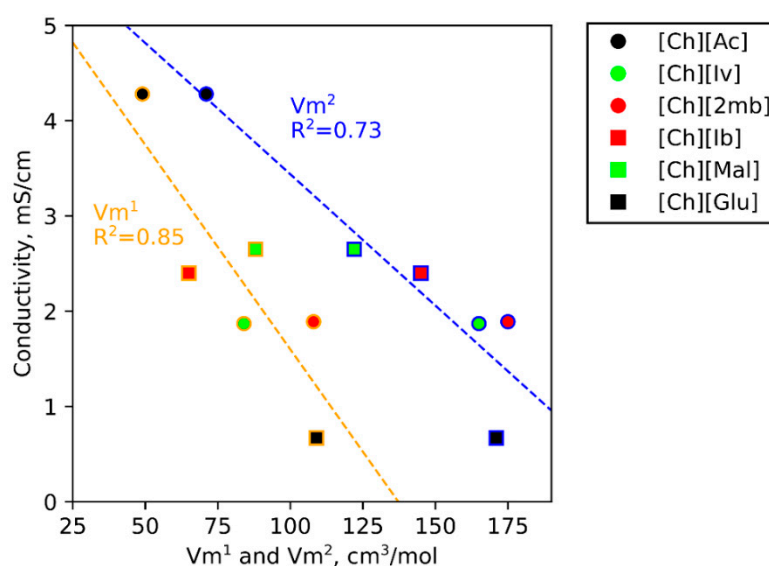


Figure 4. The correlation between the ionic conductivity of ILs after 3 weeks in ambient conditions [15] and the anion size calculated with two different methods.

Hence, to explain the severe variance in the strain differences, we hypothesized that the mobile particles to consider are not necessarily the single cations but rather the clusters of ions. Previous studies of the close-range structure of choline-based ionic liquids have indicated the presence of correlated anion-anion and cation-cation complexes [51–56]. Russina et al. performed an MD study and noted the importance of cation-cation interactions in choline amino acid anion ILs [51]. The cation-cation correlation is particularly strong due to the interaction between the ammonium and hydroxyl groups of choline. There has also been spectroscopic evidence for strong cation-cation clustering in [Ch][TFSI] [52] and [Ch][BF₄] [53].

Figures 5 and 6 present the radial distribution functions, $g(r)$ s, of cation–cation, anion–cation, and cation-choline O-H. For ILs, the normalized $g(r)$ can be approximated with an exponentially fading cosine function: $g(r) \approx -A \cdot \cos(\omega r) \cdot \exp(-\kappa r) + 1$, where A and ω are parameters that determine the height and frequency of $g(r)$ maxima, and κ is the fading rate coefficient. The variance in the maxima heights across the different ILs is caused by the competition between steric effects and various interactions, including Coulomb attraction/repulsion as well as hydrogen bonding. That is why the first cation–cation $g(r)$ maxima do not differentiate the studied ILs (e.g., [Ch][2mb], [Ch][Ib], [Ch][Glu] in Figure 5). Furthermore, the $g(r)$ of [Ch][Iv] has an atypical form with an anomalously low first peak, as shown in Figure 5 for cation-choline $g(r)$ and in Figure 6 for choline O-H $g(r)$. It is worth noting that in Figure 6, the distance between the nearest cation-choline O-H is lower than the average distance between cation-anion, which indicates the presence of strong hydrogen bonding between choline cations. Due to the competition between the cation-anion and hydrogen bonding, the usual sine-like exponentially fading form of the $g(r)$ function is distorted for the first shell (especially for [Ch][Iv]). Still, it is restored starting from the second shell.

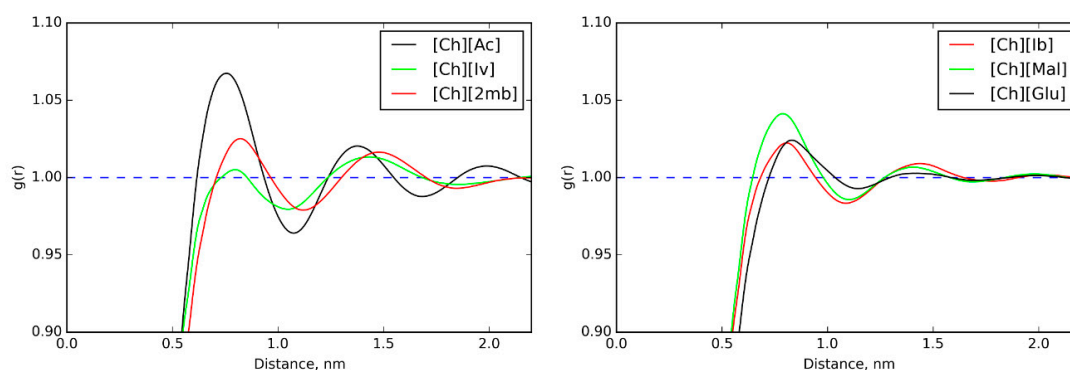


Figure 5. Cation-cation radial distribution functions, $g(r)$, calculated from the molecular dynamics trajectory data.

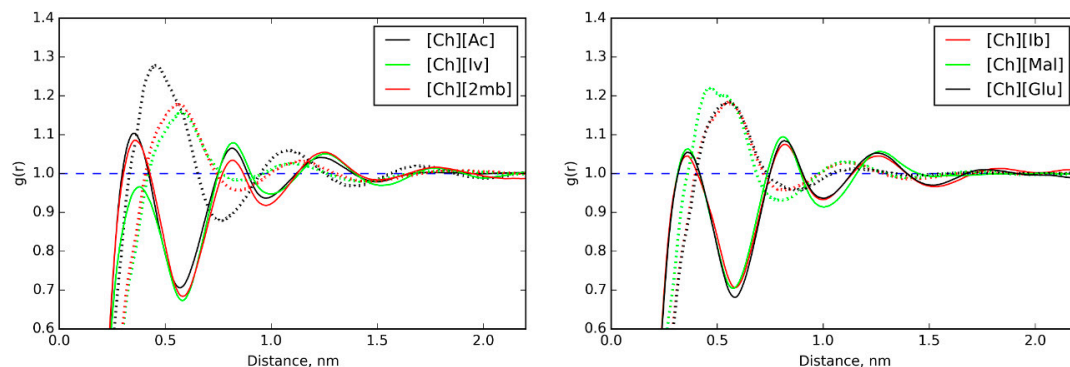


Figure 6. Radial distribution functions, $g(r)$, of cation-anion correlation (dotted line) and cation-choline O-H correlation (solid line) calculated from the molecular dynamics trajectory data.

It is reasonable to assume that the strain difference can be related to the fading rate coefficient that essentially is an inverse length of the shelled cluster. Taking into account that the number of solvation shells must be an integer, it is most convenient to operate with the second maxima heights and turn it into the potential engendered by the choline at the second $g(r)$ maxima as $U(r) = -kT \cdot \ln(g(r))$, where kT is the product of the Boltzmann constant and the temperature. As shown in Figure 7, the natural logarithm of the height of the second maxima values correlates very strongly with the experimental strain difference of PPy-PVdF actuators in the case of square wave potential driving. That supports the hypothesis that the actuation is not caused by the number of migrated ions but rather by the characteristics of the solvation shells formed by these ions. Especially in the case of driving by square wave potential, as in this regime, the target potential is set abruptly, without a ramp—like in the case of CV. Naturally, wider and stiffer solvation shells would have a much stronger mechanical interaction with the neighboring polymer chains, resulting in actuation. In PPy-gelatin actuators, a more complex interplay of interactions arises due to the hydrogen bonding properties of the membrane. Thus, the strains cannot be meaningfully correlated without simulating the ionic liquid in the full realistic polymer matrix. The evidence of strong hydrogen bonding between the choline quaternary ammonium cation and O-H in choline was found from the $g(r)$ s (Figure 6). While a decrease in ionic conductivity that comes hand in hand with the stronger hydrogen bonding [52] is not a desirable property for an actuator, the potential engendered by the choline at the second $g(r)$ maxima correlates with an increase in strain difference, as can be concluded from the unison of the experimental results and the MD simulations.

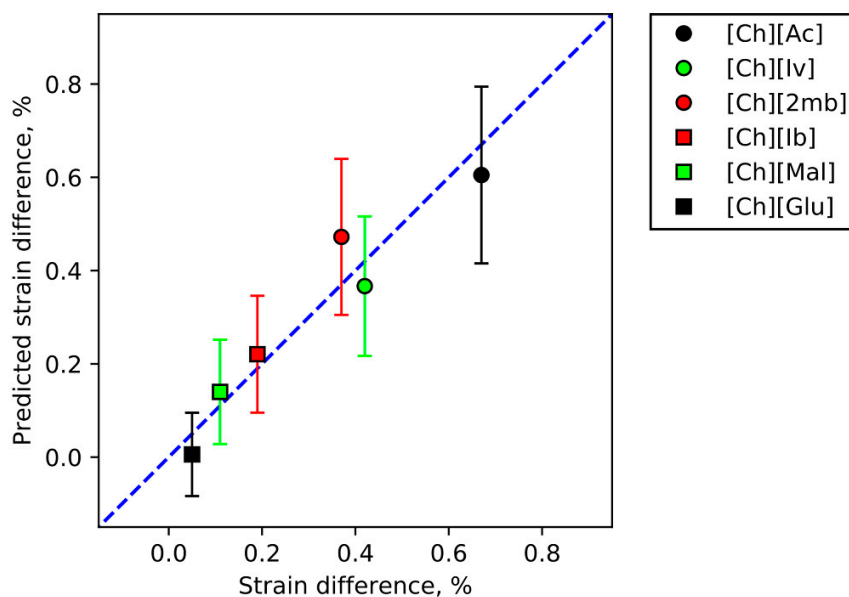


Figure 7. The measured strain differences of PPy-PVdF actuators vs the strain differences predicted by the cation-cation correlation peak height. Error bars correspond to ± 1 standard error. R^2 0.920, slope 34.465, intercept -0.089 .

4. Conclusions

The main aim of this study was to fabricate a functioning trilayered actuator using only harmless materials and to prove the harmless nature in model systems (i.e., *E. coli*) using the disk-diffusion method. In order to establish the most optimal candidates for the electrolyte, MD simulations were carried out, enabling light to be shed on the ionic clustering. The PPy-gelatin actuator with choline ILs outperformed the reference actuator combining imidazolium-based ionic liquid with PPy-gelatin. Electro-chemo-mechanical characterization revealed that gelatin membranes are more effective than PVdF in combination with PPy and choline ILs, especially with choline acetate and choline isobutyrate. This was largely due to the higher elasticity of the membrane and ionic conductivity of

the electrolyte. The disk diffusion test showed no adverse effects of PPy-gelatin actuators on *E. coli*. Computational analysis was used to explain the experimental results, revealing a strong cation–cation correlation in ILs. Cation-cation correlation peak height was found to be a good predictor of strain difference. Thus, we conclude that the mobile particles in our systems are positive clusters. As the cluster parameters are governed by both cation and anion, each IL behaves differently.

Supplementary Materials: The following are available online at <http://www.mdpi.com/2076-0825/9/2/40/s1>, Figure S1: The unit cell, which contains 400 [Ch][Ac] ion pairs and 207 water molecules (to reproduce the mass content of water—5.4%). Isometric periodic boundary conditions were applied, Figure S2: Five cations and three anions of [Ch][Ac] and two water molecules cut from the Molecular Dynamics trajectory. The H-bonds between choline cations are depicted as green, Figure S3: A fusion of partially dried fibers in the gelatin membrane, Figure S4: An example of a frequency response graph of PPy-gelatin-[Ch][Ib] actuator, Figure S5: An example of a frequency response graph of PPy-gelatin-[Ch][Mal] actuator.

Author Contributions: Conceptualization, T.T., K.P.-E., and V.I.; methodology, T.T., V.I., F.E., K.K., and P.R.; software, K.K. and V.I.; validation, F.E., K.K., P.R., and V.I.; formal analysis, F.E., K.K., and P.R.; investigation, F.E., K.K., P.R., and K.-A.N.; resources, V.I., K.P.-E., A.A., T.T., and M.J.; data curation, F.E., K.K., V.I., and P.R.; writing—original draft preparation, F.E., T.T., K.P.-E., K.K., V.I., and P.R.; writing—review and editing, T.T., K.P.-E., F.E., K.K., V.I., and P.R.; visualization, F.E., K.K., and V.I.; supervision, T.T., K.P.-E., V.I. and M.J.; project administration, K.P.-E., V.I., T.T., A.A. and M.J.; funding acquisition, K.P.-E., A.A., V.I. and T.T. All authors have read and agreed to the published version of the manuscript.

Funding: This research was funded by the European Union’s Horizon 2020 research and innovation program under the Marie Skłodowska-Curie grant agreement No 793377. The work was partially supported by the Graduate School of Functional Materials and Technologies receiving funding from the European Regional Development Fund, Estonian Research Council grant No. 772 and Institute of Technology basic funding grant 20907, as well as Estonian Personal Research Projects PUT1107 and PSG249. The computations were conducted in part in the High-Performance Computing Center of the University of Tartu.

Acknowledgments: The authors would like to thank Niilo Kaldalu for the help with disk diffusion tests and Urmas Johanson for fruitful discussions.

Conflicts of Interest: The authors declare no conflict of interest.

References

1. Temmer, R.; Maziz, A.; Plesse, C.; Aabloo, A.; Vidal, F.; Tamm, T. In search of better electroactive polymer actuator materials: PPy versus PEDOT versus PEDOT-PPy composites. *Smart Mater. Struct.* **2013**, *22*, 104006. [[CrossRef](#)]
2. Maziz, A.; Plesse, C.; Soyer, C.; Cattan, E.; Vidal, F. Top-down Approach for the Direct Synthesis, Patterning, and Operation of Artificial Micromuscles on Flexible Substrates. *ACS Appl. Mater. Interfaces* **2016**, *8*, 1559–1564. [[CrossRef](#)] [[PubMed](#)]
3. Yan, Y.; Santaniello, T.; Bettini, L.G.; Minnai, C.; Bellacicca, A.; Porotti, R.; Denti, I.; Faraone, G.; Merlini, M.; Lenardi, C.; et al. Electroactive Ionic Soft Actuators with Monolithically Integrated Gold Nanocomposite Electrodes. *Adv. Mater.* **2017**, *29*, 1606109. [[CrossRef](#)] [[PubMed](#)]
4. Mirfakhrai, T.; Madden, J.D.; Baughman, R.H. Polymer artificial muscles. *Mater. Today* **2007**, *10*, 30–38. [[CrossRef](#)]
5. Kruusamäe, K.; Punning, A.; Aabloo, A.; Asaka, K. Self-Sensing Ionic Polymer Actuators: A Review. *Actuators* **2015**, *4*, 17–38. [[CrossRef](#)]
6. Bar-Cohen, Y. *Artificial Muscles Using Electroactive Polymers (EAP): Capabilities, Challenges and Potential*; Jet Propulsion Laboratory, National Aeronautics and Space Administration: Pasadena, CA, USA, 2005; pp. 1–14.
7. Chambers, L.D.; Winfield, J.; Ieropoulos, I.; Rossiter, J. Biodegradable and edible gelatine actuators for use as artificial muscles. In *Electroactive Polymer Actuators and Devices (EAPAD) 2014*; Bar-Cohen, Y., Ed.; International Society for Optics and Photonics: San Diego, CA, USA, 2014; p. 90560B.
8. Cai, Z.; Kim, J. Characterization and electromechanical performance of cellulose–chitosan blend electro-active paper. *Smart Mater. Struct.* **2008**, *17*, 035028. [[CrossRef](#)]
9. Kim, J.; Yun, S.; Mahadeva, S.K.; Yun, K.; Yang, S.Y.; Maniruzzaman, M. Paper Actuators Made with Cellulose and Hybrid Materials. *Sensors* **2010**, *10*, 1473–1485. [[CrossRef](#)]

10. Kai, D.; Prabhakaran, M.P.; Jin, G.; Ramakrishna, S. Biocompatibility evaluation of electrically conductive nanofibrous scaffolds for cardiac tissue engineering. *J. Mater. Chem. B* **2013**, *1*, 2305. [[CrossRef](#)]
11. Siimon, K.; Siimon, H.; Järvekülg, M. Mechanical characterization of electrospun gelatin scaffolds cross-linked by glucose. *J. Mater. Sci. Mater. Med.* **2015**, *26*. [[CrossRef](#)]
12. Wang, X.; Gu, X.; Yuan, C.; Chen, S.; Zhang, P.; Zhang, T.; Yao, J.; Chen, F.; Chen, G. Evaluation of biocompatibility of polypyrrole in vitro and in vivo. *J. Biomed. Mater. Res. A* **2004**, *68*, 411–422. [[CrossRef](#)]
13. George, P.M.; Lyckman, A.W.; LaVan, D.A.; Hegde, A.; Leung, Y.; Avasare, R.; Testa, C.; Alexander, P.M.; Langer, R.; Sur, M. Fabrication and biocompatibility of polypyrrole implants suitable for neural prosthetics. *Biomaterials* **2005**, *26*, 3511–3519. [[CrossRef](#)] [[PubMed](#)]
14. Egorova, K.S.; Ananikov, V.P. Toxicity of Ionic Liquids: Eco(cyto)activity as Complicated, but Unavoidable Parameter for Task-Specific Optimization. *ChemSusChem* **2014**, *7*, 336–360. [[CrossRef](#)] [[PubMed](#)]
15. Elhi, F.; Priks, H.; Rinne, P.; Kaldalu, N.; Žusinaite, E.; Johanson, U.; Aabloo, A.; Tamm, T.; Põhako-Esko, K. Electromechanically active polymer actuators based on biofriendly choline ionic liquids. *Smart Mater. Struct.* **2020**. [[CrossRef](#)]
16. Kaynak, A.; Yang, C.; Lim, Y.C.; Kouzani, A. Electrochemical fabrication and modelling of mechanical behavior of a tri-layer polymer actuator. *Mater. Chem. Phys.* **2011**, *125*, 113–117. [[CrossRef](#)]
17. Liu, S.; Masurkar, N.; Varma, S.; Avrutsky, I.; Reddy Arava, L.M. Experimental Studies and Numerical Simulation of Polypyrrole Trilayer Actuators. *ACS Omega* **2019**, *4*, 6436–6442. [[CrossRef](#)] [[PubMed](#)]
18. Nguyen, C.H.; Alici, G.; Wallace, G.G. Modelling trilayer conjugated polymer actuators for their sensorless position control. *Sens. Actuators Phys.* **2012**, *185*, 82–91. [[CrossRef](#)]
19. Farajollahi, M.; Madden, J.D.W.; Sassani, F. Non-linear time variant model intended for polypyrrole-based actuators. In *Electroactive Polymer Actuators and Devices (EAPAD) 2014*; Bar-Cohen, Y., Ed.; International Society for Optics and Photonics: San Diego, CA, USA, 2014; p. 90561T.
20. Ikushima, K.; John, S.; Yokoyama, K.; Nagamitsu, S. A practical multilayered conducting polymer actuator with scalable work output. *Smart Mater. Struct.* **2009**, *18*, 095022. [[CrossRef](#)]
21. Lopez Cascales, J.J.; Otero, T.F. Understanding the structural changes that take place in a polypyrrole film during its oxi-reduction process: A molecular dynamics simulation study. In *Nanotechnology II*; Lugli, P., Kish, L.B., Mateos, J., Eds.; International Society for Optics and Photonics: Sevilla, Spain, 2005; p. 258.
22. López Cascales, J.J.; Otero, T.F. Molecular dynamic simulation of the hydration and diffusion of chloride ions from bulk water to polypyrrole matrix. *J. Chem. Phys.* **2004**, *120*, 1951–1957. [[CrossRef](#)]
23. Otero, T.F.; Lopez Cascales, J.J. *Modeling the Polypyrrole Water Interface by Molecular Dynamics Simulation*; Bar-Cohen, Y., Ed.; International Society for Optics and Photonics: San Diego, CA, USA, 2004; p. 164.
24. López Cascales, J.J.; Fernández, A.J.; Otero, T.F. Characterization of the Reduced and Oxidized Polypyrrole/Water Interface: A Molecular Dynamics Simulation Study. *J. Phys. Chem. B* **2003**, *107*, 9339–9343. [[CrossRef](#)]
25. Takeuchi, I.; Asaka, K.; Kiyohara, K.; Sugino, T.; Terasawa, N.; Mukai, K.; Fukushima, T.; Aida, T. Electromechanical behavior of fully plastic actuators based on bucky gel containing various internal ionic liquids. *Electrochim. Acta* **2009**, *54*, 1762–1768. [[CrossRef](#)]
26. Kwon, K.-S.; Ng, T.N. Improving electroactive polymer actuator by tuning ionic liquid concentration. *Org. Electron.* **2014**, *15*, 294–298. [[CrossRef](#)]
27. Davidson, J.D.; Goulbourne, N.C. Boundary layer charge dynamics in ionic liquid-ionic polymer transducers. *J. Appl. Phys.* **2011**, *109*, 014909. [[CrossRef](#)]
28. Siimon, K.; Mõisavald, K.; Siimon, H.; Järvekülg, M. Increasing mechanical strength of electrospun gelatin nanofibers by the addition of aluminum potassium sulfate. *J. Appl. Polym. Sci.* **2015**, *132*, 1–5. [[CrossRef](#)]
29. Temmer, R.; Must, I.; Kaasik, F.; Aabloo, A.; Tamm, T. Combined chemical and electrochemical synthesis methods for metal-free polypyrrole actuators. *Sens. Actuators B Chem.* **2012**, *166–167*, 411–418. [[CrossRef](#)]
30. Sugino, T.; Kiyohara, K.; Takeuchi, I.; Mukai, K.; Asaka, K. Actuator properties of the complexes composed by carbon nanotube and ionic liquid: The effects of additives. *Sens. Actuators B Chem.* **2009**, *141*, 179–186. [[CrossRef](#)]
31. Klesewetter, L.; Houdeau, D.; Steckenbom, A. Determination of Young's moduli of micromechanical thin films using the resonance method. *Sens. Actuators Phys.* **1992**, *32*, 153–159. [[CrossRef](#)]
32. Bauer, A.W.; Kirby, W.M.M.; Sherris, J.C.; Turck, M. Antibiotic Susceptibility Testing by a Standardized Single Disk Method. *Am. J. Clin. Pathol.* **1966**, *45*, 493–496. [[CrossRef](#)]

33. Hudzicki, J. *Kirby-Bauer Disk Diffusion Susceptibility Test Protocol*; American Society for Microbiology: Washington, DC, USA, 2009.
34. Abraham, M.J.; Murtola, T.; Schulz, R.; Páll, S.; Smith, J.C.; Hess, B.; Lindahl, E. GROMACS: High performance molecular simulations through multi-level parallelism from laptops to supercomputers. *SoftwareX* **2015**, *1–2*, 19–25. [[CrossRef](#)]
35. Jorgensen, W.L.; Maxwell, D.S.; Tirado-Rives, J. Development and Testing of the OPLS All-Atom Force Field on Conformational Energetics and Properties of Organic Liquids. *J. Am. Chem. Soc.* **1996**, *118*, 11225–11236. [[CrossRef](#)]
36. Martínez, L.; Andrade, R.; Birgin, E.G.; Martínez, J.M. PACKMOL: A package for building initial configurations for molecular dynamics simulations. *J. Comput. Chem.* **2009**, *30*, 2157–2164. [[CrossRef](#)]
37. Darden, T.; York, D.; Pedersen, L. Particle mesh Ewald: An N -log(N) method for Ewald sums in large systems. *J. Chem. Phys.* **1993**, *98*, 10089–10092. [[CrossRef](#)]
38. Berendsen, H.J.C.; Postma, J.P.M.; van Gunsteren, W.F.; DiNola, A.; Haak, J.R. Molecular dynamics with coupling to an external bath. *J. Chem. Phys.* **1984**, *81*, 3684–3690. [[CrossRef](#)]
39. Breneman, C.M.; Wiberg, K.B. Determining atom-centered monopoles from molecular electrostatic potentials. The need for high sampling density in formamide conformational analysis. *J. Comput. Chem.* **1990**, *11*, 361–373. [[CrossRef](#)]
40. Perdew, J.P.; Burke, K.; Ernzerhof, M. Generalized gradient approximation made simple. *Phys. Rev. Lett.* **1996**, *77*, 3865–3868. [[CrossRef](#)] [[PubMed](#)]
41. Weigend, F.; Ahlrichs, R. Balanced basis sets of split valence, triple zeta valence and quadruple zeta valence quality for H to Rn: Design and assessment of accuracy. *Phys. Chem. Chem. Phys.* **2005**, *7*, 3297–3305. [[CrossRef](#)] [[PubMed](#)]
42. Weigend, F. Accurate Coulomb-fitting basis sets for H to Rn. *Phys. Chem. Chem. Phys.* **2006**, *8*, 1057–1065. [[CrossRef](#)]
43. Neese, F. The ORCA program system. *Wiley Interdiscip. Rev. Comput. Mol. Sci.* **2012**, *2*, 73–78. [[CrossRef](#)]
44. Grimme, S.; Bannwarth, C.; Shushkov, P. A Robust and Accurate Tight-Binding Quantum Chemical Method for Structures, Vibrational Frequencies, and Noncovalent Interactions of Large Molecular Systems Parametrized for All spd-Block Elements ($Z = 1–86$). *J. Chem. Theory Comput.* **2017**, *13*, 1989–2009. [[CrossRef](#)]
45. Frisch, M.J.; Trucks, G.W.; Schlegel, H.B.; Scuseria, G.E.; Robb, M.A.; Cheeseman, J.R.; Scalmani, G.; Barone, V.; Mennucci, B.; Peterson, G.A.; et al. *Gaussian 09*; Gaussian, Inc.: Wallingford, CT, USA, 2009.
46. Becke, A.D. Density-functional thermochemistry. III. The role of exact exchange. *J. Chem. Phys.* **1993**, *98*, 5648–5652. [[CrossRef](#)]
47. Lee, C.; Yang, W.; Parr, R.G. Development of the Colle-Salvetti correlation-energy formula into a functional of the electron density. *Phys. Rev. B* **1988**, *37*, 785. [[CrossRef](#)]
48. Humphrey, W.; Dalke, A.; Schulten, K. VMD: Visual molecular dynamics. *J. Mol. Graph.* **1996**, *14*, 33–38. [[CrossRef](#)]
49. Bondi, A. van der Waals Volumes and Radii. *J. Phys. Chem.* **1964**, *68*, 441–451. [[CrossRef](#)]
50. Karu, K.; Elhi, F.; Pöhako-Esko, K.; Ivaništšev, V. Predicting Melting Points of Biofriendly Choline-Based Ionic Liquids with Molecular Dynamics. *Appl. Sci.* **2019**, *9*, 5367. [[CrossRef](#)]
51. Russina, O.; Santis, S.D.; Gontrani, L. Micro-and mesoscopic structural features of a bio-based choline- amino acid ionic liquid. *RSC Adv.* **2016**, *6*, 34737–34743. [[CrossRef](#)]
52. Knorr, A.; Fumino, K.; Bónsa, A.-M.; Ludwig, R. Spectroscopic evidence of cholinium ‘jumping and pecking’ and H-bond enhanced cation-cation interaction in ionic liquids. *Phys. Chem. Chem. Phys.* **2015**, *17*, 30978–30982. [[CrossRef](#)]
53. Knorr, A.; Ludwig, R. Cation-cation clusters in ionic liquids: Cooperative hydrogen bonding overcomes like-charge repulsion. *Sci. Rep.* **2015**, *5*, 1–7. [[CrossRef](#)] [[PubMed](#)]
54. Campetella, M.; Le Donne, A.; Daniele, M.; Gontrani, L.; Lupi, S.; Bodo, E.; Leonelli, F. Hydrogen Bonding Features in Cholinium-Based Protic Ionic Liquids from Molecular Dynamics Simulations. *J. Phys. Chem. B* **2018**, *122*, 2635–2645. [[CrossRef](#)]

55. Le Donne, A.; Adenusi, H.; Porcelli, F.; Bodo, E. Hydrogen Bonding as a Clustering Agent in Protic Ionic Liquids: Like-Charge vs. Opposite-Charge Dimer Formation. *ACS Omega* **2018**, *3*, 10589–10600. [[CrossRef](#)]
56. Gamrad, W.; Dreier, A.; Goddard, R.; Pörschke, K.-R. Selbstassoziation organischer Kationen über N-C-H...O-Wasserstoffbrückenbindungen. *Angew. Chem.* **2015**, *127*, 4564–4569. [[CrossRef](#)]



© 2020 by the authors. Licensee MDPI, Basel, Switzerland. This article is an open access article distributed under the terms and conditions of the Creative Commons Attribution (CC BY) license (<http://creativecommons.org/licenses/by/4.0/>).